IRIS AperTO

UNIVERSITÀ DEGLI STUDI DI TORINO

AperTO - Archivio Istituzionale Open Access dell'Università di Torino

Photocatalytic performances of rare earth element-doped zinc oxide toward pollutant abatement in water and wastewater

This is the author's manuscript

Original Citation:

Availability:

This version is available http://hdl.handle.net/2318/1689456 since 2021-03-09T15:13:50Z

Published version:

DOI:10.1016/j.apcatb.2018.12.053

Terms of use:

Open Access

Anyone can freely access the full text of works made available as "Open Access". Works made available under a Creative Commons license can be used according to the terms and conditions of said license. Use of all other works requires consent of the right holder (author or publisher) if not exempted from copyright protection by the applicable law.

(Article begins on next page)

08 November 2026

Photocatalytic performances of rare earth element-doped zinc oxide toward pollutant abatement in water and wastewater

Fabrizio Sordello, Ilaria Berruti, Chiara Gionco, Maria Cristina Paganini, Paola Calza*, Claudio Minero

Università degli Studi di Torino, Dipartimento di Chimica, via P. Giuria 5, 10125 Torino, Italy

*corresponding author: paola.calza@unito.it

Abstract

The photocatalytic performance of pristine and rare earth elements (La, Ce, Pr, Er, Yb) doped zinc oxide was tested toward the abatement of a model pollutant in MilliQ water and wastewater matrices. ZnO doped with Ce, Er and particularly with Yb exhibited photoactivity higher than bare zinc oxide and the benchmark TiO_2 P25, especially in wastewater matrix. Several electrochemical investigations were performed *via* chronopotentiometry and cyclic voltammetry aimed to shed light on the reasons why the diverse materials behaved differently. From the overall data a complex picture emerged, where there is not a single property of the materials evidently outperforming the others. Nonetheless, from the analysis of whole data a limited role of doping emerged for La and Pr, doping with Er improved the photocurrent, doping with Yb favoured a better accumulation of photoelectrons, and doping with Ce promoted a faster electron transfer.

Keywords: zinc oxide, rare earth doping, wastewater, pollutant abatement, PLS

1. Introduction

Among semiconductor nanomaterials, ZnO has several interesting properties and broad applications. Photocatalysts based on semiconductors are widely used in the conversion of light energy into useful chemical energy. ZnO is considered as a benchmark catalyst due to its non-toxic nature coupled with low cost [1]. One major drawback of existing technology is the low quantum efficiency of ZnO, which is due to very fast recombination of photogenerated electron–hole pairs. In order to improve the photocatalytic activity of ZnO, several modification methods have been developed. It has been reported that photocatalytic performance of semiconductor photocatalyst can be improved by doping with certain cations which can act as electron trapping agent to decrease the electron hole recombination rate [2, 3].

A possible way to improve the photocatalytic activity is the formation of semiconductor-semiconductor p−n heterojunctions. It was found that the p−n junctions formed in combination with both p-type and n-type semiconductors can effectively reduce the recombination rate of the photogenerated electron/hole pairs, with consequent enhancement of the photocatalytic activity [4-7]. More recently, our and other research groups started to investigate the role of rare earth elements (RE = La, Ce, Pr, Er and Yb) as dopant of different oxides [8-10]. In a very recent paper we demonstrated that the presence in the mixed material of CeO_2/ZnO interfaces appears responsible of specific photochemical properties [11]. The material is composed of segregated CeO_2 nanoparticles supported on larger ZnO nanostructures. Nevertheless, the presence of relatively low amounts of Ce (1%) were able to modify radically the behavior under irradiation. This effect has been explained in terms of alignment of bands of the two different oxide phases respectively, with the electron transfer from one species to the other helping the charge separation effect.

In previous papers [12, 13] we prepared pure and doped ZnO with low Ce loading (1% molar) *via* hydrothermal process, a low temperature, green and simple process to obtain controlled nanostructures, starting from different precursors. The specific percentage of 1% molar of dopant was chosen according to the best photocatalytic results obtained. The photocatalytic activity of the synthesized materials was tested on phenol [13] and on more refractory compounds, such as iodinated X-ray contrast agents (ICM) [2], which are emerging contaminants, known to be scarcely abated in the wastewater treatment plants. Also in this case the achievement of the fast drug disappearance was a great success. [13] The same material has been successfully used in the abatement of acesulfame K, an artificial sweetener [12, 13].

Based on these very encouraging results, in a recent study we extended the investigation to other rare earth elements (RE = La, Ce, Pr, Er and Yb). We synthesized *via* hydrothermal process and characterized different photocatalysts based on ZnO doped with a low amount of RE (1% molar). [14-18]

In the present paper, we tested their photocatalytic performances toward a model pollutant, phenol, in different matrices, namely MilliQ water and wastewater, to assess if the higher activity is still maintained when facing with very complex and challenging matrices. Furthermore, through a comprehensive electrochemical investigation and statistical analysis we were able to correlate the improved activity with the different parameters affecting the photocatalytic process.

2. Experimental section

2.1. Materials

All reactants employed in this work were purchased from Aldrich with purity higher than 99.9% and were used without any further purification treatment. Bare ZnO sample was synthesized starting from a 1 M water solution of $Zn(NO_3)_2 \cdot 6H_2O$. Then a 4 M NaOH solution was added until the pH was 10-11, and finally the solution was transferred into a PTFE lined stainless steel 100 mL autoclave (filling 70%), then treated at 175°C overnight. The product was centrifuged and washed with deionized water, then dried at 70°C. The doped ZnO samples with rare earth elements RE 1% molar were prepared adding the stoichiometric amount of RE chlorides in the starting solution, then the same procedure described in [14] has been followed. The samples will be labelled as ZnO, ZnO-Ce, ZnO-La, ZnO-Yb, ZnO-Pr and ZnO-Er.

TiO_2 P25 Evonik was used as benchmark photocatalyst, after being irradiated and washed with ultrapure water in order to eliminate the potential interference caused by adsorbed ions such as chloride, sulphate and sodium.

Phenol (P), catechol (CAT), hydroquinone, methanol (≥99.9%), acetonitrile (≥99.9%) and formic acid(99%) were purchased from Sigma Aldrich (Milan, Italy). HPLC grade water was obtained from MilliQ System Academic (Waters, Millipore). HPLC grade methanol (BDH) and acetonitrile (Aldrich) were filtered through a 0.45 μm filter before use. Effluent and influent wastewaters (EWW and IWW, respectively) were provided by ACEA Pinerolese (Italy, a standard treatment plant). Total organic carbon measured was 12.96 mg L^{-1} and the pH was 8.05.

2.2. Materials characterization

SEM, TEM, XRD and BET DR-UV-Vis results were reported and deeply discussed in a previous paper. [14] Here we remind that the specific surface area (< 10 m^2 g^{-1}) is very similar for all samples, as the UV-Vis spectra, indicating that the RE insertion does not directly affect the VB → CB transition. Nevertheless, in the case of samples containing Pr, Er and Yb it is possible to detect the presence of a multitude of defined absorption bands, related to the f-f transitions of Pr, Er and Yb ion states. The presence of these bands indicates that the RE ions are well diluted in the matrix.

2.3. Photocatalytic tests

Irradiation experiments were carried out using air-saturated Pyrex glass cells filled with 5 mL of the solution of the target molecule. The concentration of phenol was 20 mg L^{-1}. The photocatalyst concentration was 1000 mg L^{-1}. Samples were irradiated using a Philips TLK/05 lamp 40 Watt with maximum emission at 365 nm. The incident irradiance was 25 W m^{-2}.

2.4. Analytical techniques

Phenol and its transformation products were monitored with a Merck-Hitachi liquid chromatograph equipped with Rheodyne injector L-6200 and L-6200A pumps for high-pressure gradients, L-4200 UV-Vis detector (the detection wavelength was set at 220 nm) and a LiChrocart RP-C18 column (Merck, 12,5 cm x 0,4 cm). Isocratic elution (1 mL min^{-1} flow rate) was carried out with 80% of phosphate buffer $1x10^{-2}$ M at pH 2.8 and 20% acetonitrile and retention times was 6.45 min.

2.5. Electrochemical tests

The electrochemical experiments were carried out with a standard photoelectrochemical set-up composed of a computer-controlled potentiostat, AUTOLAB PGSTAT12, and a 150 W LOT Oriel Xe arc lamp as radiation source. The incident irradiance on the sample was 84 W m^{-2} in the 250-400 nm range. The electrochemical cell was a conventional three-electrode cell, in which the counter and reference electrodes were a Pt sheet and an Ag/AgCl/KCl 3 M electrode, respectively. If needed the electrolytic solution was purged with nitrogen or oxygen gas with purity 99.9999% obtained from Sapio (Italy). Transparent conductive supports (Corning® EXG alkaline earth boro-aluminosilicate glass, 25 x 25 x 1.1 mm, coated with Indium Tin Oxide on one surface, R_s = 9 - 15 Ω/□, Transmission >80%) were obtained from Delta Technologies Ltd (USA). In all cases electrolyte was KNO_3 100 mM with K_2HPO_4 10 mM at pH 8.85±0.05.

2.6. Electrode preparation

Working electrodes were prepared with doctor blade technique. The semiconductor powders were mixed with MilliQ® water to obtain slurries, and then deposited onto the conductive supports using adhesive tape as a spacer and a microscope slide to spread the slurry. In this way 20±5 mg of semiconductor were deposited on each electrode. Copper foil tape with conductive adhesive (RS Components, UK) was used to solder a copper wire and ensure the electric contact. The electric contact was insulated with black epoxy resin (RS Components, UK) to avoid its corrosion during electrochemical measurements. The area of the semiconductor coated surface was 2.25 cm^2.

3. Results

3.1. Photocatalytic test on phenol

The photocatalytic activity of pristine and rare earth elements doped ZnO-based materials was tested using phenol as probe molecule. Adsorption experiments in the dark were performed in a 2 h time window and showed that phenol was poorly adsorbed on all materials as adsorption was always below 10%. Direct photolysis scarcely contributed to phenol transformation even after long irradiation times.

3.1.1. Tests in MilliQ water

The time evolution of phenol in MilliQ water in the presence of bare and rare earth elements doped ZnO is reported in Figure 1. For comparison purpose, the degradation performed under the same conditions with the benchmark TiO_2 P25 is shown as well. The degradation efficiency was very similar for P25 and bare ZnO, while some difference arose for doped materials. Doping with lanthanum exhibited a slight detrimental effect, while ZnO doped with cerium, erbium and ytterbium showed enhanced degradation rates. The degradation curve approximated a pseudo-first-order kinetics and we calculated the kinetic constants, which are collected in Figure 2. Excluding the case of cerium, the rate constant value seems related to the number of electrons present in the f orbitals as the rate increases with increasing atomic number Z. The diverse behavior of Ce-doped ZnO could be due to the different structure of this sample [14] and, in particular, to the formation of two distinct phases, clearly observable in both XRD and TEM measurements, which are not present with other doping elements.

Phenol transformation is known to occur through the formation of hydroxyl derivatives, i.e. catechol (CAT), hydroquinone (HQ), 1,4-benzoquinone, resorcinol and, in a slight extent, of condensed products.[19] In our experimental conditions, the intermediates were identified as HQ and CAT. In all cases, the time evolution follows a typical bell-shaped profile, and differences arose from their net rate of formation-disappearance when using TiO_2 and ZnO-based materials (Figure S1). In the case of P25, HQ was identified at high amount (2.5 mg L^{-1}), while CAT was detected at very low concentration (0.2 mg L^{-1}), due to the strong adsorption of catechol on the catalyst surface.[20, 21] This phenomenon was evidently less important for ZnO based material as CAT and HQ were detected at comparable concentrations.

The maximum yield of CAT and HQ was reached with ZnO-Ce, ZnO-Er and ZnO-Yb in 15-20 min and then almost 50% disappeared within 1 h of irradiation. The evolution rate was slowed down with ZnO, ZnO-La and ZnO-Pr, the largest concentrations were achieved after 30 min and they did not significantly decrease in the considered time window.

3.1.2. Tests in influent and effluent wastewaters

The time evolution for phenol in the presence of the catalysts in EWW and IWW are plotted in Figure 1, together with the degradation profile obtained with the benchmark P25. In EWW, phenol was only partially degraded with P25, while it was completely degraded with ZnO based materials. In particular, the degradation was favored with ZnO-Yb and ZnO-Er. In IWW the rates were always slower than in EWW and MilliQ water. The different performances of tested materials were even more marked with the following order: ZnO-Yb, ZnO-Er> ZnO-Ce> ZnO-Pr>ZnO-La>ZnO. This trend, already observed in MilliQ water, seems correlated to the atomic number, and then to the decrease of the ionic radius, with ZnO-Ce only exception.[14]

The calculated kinetic constants in the different matrices are collected in Figure 2. It can be noted that all zinc-based materials exhibited higher efficiency than P25. In MilliQ water, all synthesized materials except ZnO-La were more efficient than P25 and, in particular, ZnO-Ce and ZnO-Yb were the most efficient at the employed catalyst loading. [14] In the experiments performed in wastewater the performance of P25 was deeply reduced, while ZnO-based materials were less influenced. Evidently, in the complex matrix typical of a wastewater, there are species that like CAT, as observed before, can complex the surface and there act as recombination centers, lowering the net photocatalytic activity.[22] Furthermore, both in EWW and in IWW the catalyst efficiency increased with atomic number as in MilliQ water.

ZnO-Er and ZnO-Yb exhibited also the most efficient abatement of the transformation products (TPs). The main TPs formed from phenol degradation were HQ and CAT and both materials were able to completely abate them within 2h (EWW) or 4h (IWW) (see Figure S2 and S3 in Supplementary data, SD). As already observed in MilliQ water, the concentration of CAT detected was very low with P25, due to the adsorption on the catalyst surface, while with ZnO-based materials the two TPs are formed at similar amounts. Considering EWW, the maximum yield of HQ and CAT was reached in 15 min with ZnO-Er and ZnO-Yb, while longer times were required for the other materials. In the cases of P25, ZnO-La and ZnO-Pr, TPs were accumulated and not completely degraded in the considered time window (Figure S2). In IWW, the maximum amount of HQ and CAT was reached in 60 min with ZnO-Yb and ZnO-Er, while up to 120 min were required for the other materials; in the case of ZnO-La, HQ did not reach the maximum in the considered time (4h, see Figure S3).

3.2. Electrochemical characterization

All the recorded and calculated electrochemical data are reported in Table 1 and their significance is explained in Table S1. The chronopotentiometry at open circuit potential (OCP) of undoped ZnO (Figure 3a) revealed marked photoactivity as witnessed by the sudden decrease of the OCP under irradiation. The measurements on other materials, which displayed similar trends, are reported in SD (Figures S4-S9). OCP decreased until a steady state value under irradiation was reached (OCP2, Table 1). This value is a function

of the electrode characteristics and electrolyte composition. Indeed, when oxygen was bubbled in the electrolyte instead of nitrogen, the OCP under irradiation stabilized to a significantly more positive value (OCP5), whereas in the presence of methanol its value was more negative (OCP3 and OCP4). When irradiation was interrupted, the OCP relaxed to the dark value over timescale of hundreds to thousands of seconds, depending again on the working electrode material and electrolyte composition. The trends could be replicated many times. We observed similar trends in the case of the doped ZnO specimens. For reference, in the case of TiO_2 P25, the OCP values in deaerated electrolytes were significantly more negative (Table 1). The OCP relaxation after irradiation with N_2 and O_2 purging, will be analyzed in the following to estimate the recombination constant of the photogenerated charge carriers and the kinetic constant for the reaction among photogenerated electrons and dissolved oxygen.

In cyclic voltammetry (CV) we observed a monotonic increase of the cathodic current density with increasingly cathodic potential, and a cathodic current peak was never reached, as observed in previous reports on semiconducting oxides.[23, 24] Conversely, we detected a marked anodic peak at -0.4 /-0.5 V (depending on the scan rate) vs Ag/AgCl for both ZnO (Figure 3b) and doped ZnO specimens (see SD for details). With O_2 purging the maximum current of the anodic peak was reduced for all the samples to less than one half compared to deaerated electrolyte, whereas the cathodic current recorded at -1 V vs Ag/AgCl increased compared to anoxic conditions, especially at lower scan rates (Figure 3c).

3.3. Discussion

The kinetic data reported in Figure 2 could be justified supposing that the rare earth-doping improves the charge carrier separation. While this abused explanation could be possible in the case of Ce-doping, where a biphasic system is present [11], it is harder to justify the better performance of the other specimens where two different phases were not detected. For these reasons we checked the possibility of surface adsorption of rare earth elements. As the proof that they are predominantly present at the surface is a difficult task, we performed photocatalytic degradation experiments in the presence of fluorides, which complex all these rare earth elements with almost the same stability constant ($\log\beta \approx 4$).[25] If the RE at the surface played a significant role during the photocatalytic degradation, then their capping with fluoride would affect the photocatalytic activity. The positive effect of fluoride on phenol photocatalytic degradation on P25 was already reported. [22] The rate increase in the presence of fluoride was attributed to the reduced adsorption of phenol degradation products, especially CAT, on P25 surface, thus limiting substrate-mediated recombination. Here, in the presence of pristine ZnO no difference was observed (see Figure S10), confirming the previous observation with CAT that ZnO surface is not prone to complexation. Moreover, also in the presence of rare earth elements, except for La and Yb, no difference was observed (see Figure S10), thus partially ruling out the hypothesis that the adsorption at the surface could play a

crucial role. For these reasons, we undertook a deep electrochemical study to possibly find the basic factors influencing the observed rates.

Cyclic voltammetry is a tool to probe the density of states (DoS) of the electrode materials as a function of the applied potential, and, therefore, to extract information about the redox potential of trap states, and of the conduction and valence band of semiconducting electrodes. Indeed, when the potential is swept toward negative values, the Fermi level in the semiconductor is displaced toward the conduction band, while it is forced toward the valence band when the potential is swept in the positive direction. When the applied potential forces the Fermi level inside the band-gap, the current density recorded is in the order of 1 μA cm^{-2} or less, because the conductivity of the material is usually low, as it is the DoS at these potential values. At energy levels close to the bands, the DoS usually increases exponentially because of the presence of more trap states. The increase becomes more dramatic when the applied potential crosses the conduction/valence band edges.[23] Nonetheless, it is not easy to determine the position of the band edges by CV, because the band pinning regime cannot be guaranteed when trap states becomes charged, i.e. exactly when the applied potential, and indeed the Fermi level, is about to reach the band edge, leading to uncertainty in the exact determination of the band edge energy. On the other hand, the determination of the trap state energy is more precise, especially in the case of deep traps, when the semiconductor is in the band-pinning regime. If there are no redox couples in solution, the charge carriers promoted into the semiconductor trap states due to the external bias cannot be transferred to the solution, and, especially if the scan rate is high, trap states can reversibly be populated and depopulated, leading to reversible voltammograms.[23] This is indeed the case of the CVs recorded under N_2 purging (Figures 3b and S4-S9 (b)), in which the anodic peak is clearly visible, whereas in the case of O_2 purging (Figure 3c and S4-S9 (c)) the marked reduction of the anodic current and the increased cathodic current witness that trapped electrons in pristine and doped ZnO materials can reduce dissolved O_2, in agreement with the results of the photocatalytic tests. To confirm that the abatement of organic molecules obtained under irradiation is due to the transfer of photogenerated charge carriers to solution species, and not to spurious effects, we performed OCP measurements to assess the charge carrier reactivity.

OCP measurements can reveal photoactivity, discriminate between n-type and p-type semiconductors and, eventually, if coupled to CV, quantify the photogenerated majority carrier density.[26] The photoactivity is present in all the materials tested, as witnessed by the difference between dark potential and its value upon irradiation (OCP1 and OCP2 in Table 1). Since in all cases the OCP equilibrated at significantly more negative values compared to dark conditions, we concluded that ZnO and doped ZnO are n-type semiconductors, and behave similarly to TiO_2 P25 (Figure 3a and Figures S4-S9 (a)). Indeed, in the case of n-type semiconductors under irradiation, holes are trapped and transferred to solution species faster than photoelectrons, which accumulate and shift the quasi Fermi level, and consequently the OCP, to more

negative potential. On the other hand, irradiating p-type semiconductors leads to hole accumulation and to a positive shift of the OCP. [24, 26] Steady state is achieved in approximately 1000-2000 s, because charge carriers generation and their loss reach the same rate when a certain photoelectron density n_{ph} is obtained. When electron and hole scavengers are not present in the electrolyte, charge carrier loss is mainly due to recombination. Therefore, in this case, when irradiation is interrupted, the OCP relaxation to its dark value gives information about the photoelectron recombination kinetics. To convert OCP values under irradiation and immediately after switching off the irradiation into photoelectron density n_{ph}, we integrated the cathodic current of the CV obtained at the fastest scan rate (200 mV s^{-1}), in order to ensure capacitive behavior, following Equation 1: [26]

$$n_{ph} = \frac{1}{e\ d\ A} \int_{E_{dark}}^{E_{light}} \frac{i}{s} dE$$

where *e* is the charge of the electron, *d* and *A* are the electrode thickness and area, respectively, *i* is the current recorded during the CV, *s* is the potential scan and E_{dark} and E_{light} are the OCP of the electrode recorded in the dark and under steady-state irradiation, respectively. The n_{ph} obtained under irradiation at steady state in deaerated ($n_{ph}2$) and in O_2-saturated electrolyte ($n_{ph}5$) are reported in Table 1. The OCP, which equilibrated at significantly more positive values in the presence of O_2; indicates that photoelectrons do not accumulate in these conditions, and demonstrates that all the materials can photo-reduce dissolved molecular oxygen. The values of n_{ph} under O_2 are lower compared to N_2 purging, usually by one order of magnitude. This evidence is coherent with CV results, where the intensity of the anodic current peak was significantly reduced in O_2 purged electrolyte.

The values of n_{ph} after light interruption were employed to compute recombination constants, k_R, in the case of deaerated electrolyte, where we assume that the main path to photoelectron decay is recombination with trapped holes. Conversely, we obtained kinetic constants for the reaction with dissolved O_2, k_{O2}, in the case of O_2-saturated electrolyte, where photoelectrons are mainly lost because of the reduction reaction of O_2. Rate constants were evaluated assuming pseudo-first order kinetics [26] following the equation:

$$k_R = \frac{1}{n_{ph}} \frac{d\, n_{ph}}{dt}$$

Table 1 reports k_R and k_{O2} values evaluated in two different conditions, i.e. at the corresponding OCP under irradiation ($k_{2,R}$ and $k_{2,O2}$), and at an arbitrary photoelectron density of 10^{17} cm^{-3}(k_R) and 10^{16} cm^{-3}($k_{1,O2}$), respectively. This has been done because k_R and k_{O2} are not necessarily constant as functions of n_{ph} and the OCP; because more negative OCP corresponds to larger photoelectron energy, and usually to increased

282 reactivity. This is the reason why k_R and k_{O2} tend to increase with increasing n_{ph} and with increasingly
283 negative OCP values [26]. We ascribed the lack of anticorrelation between k_R and n_{ph} in deaerated
284 electrolytes to this effect. The OCP relaxation kinetics once irradiation is interrupted were significantly
285 faster in O_2-purged electrolytes compared to deaerated solution for all the materials considered, as
286 witnessed by the difference between k_R and k_{O2}, which is of two orders of magnitude for most of the
287 specimens, with the notable exception of ZnO-Er and TiO_2 P25, which appear to be the least reactive
288 materials with dissolved O_2 ($k_{1,O2}$ and $k_{2,O2}$ in Table 1). We can therefore conclude that photoelectron
289 reaction with dissolved O_2 is faster than recombination with trapped holes for all the materials here
290 presented, an essential feature for an efficient photocatalyst. This is even more pronounced in the case of
291 the ZnO specimens compared to TiO_2 P25.

292 Nevertheless, the above results are not sufficient to explain the photocatalytic activity in the degradation of
293 pollutants. The photocatalytic process is complex, and the overall rate is the result of the interplay among
294 several processes, (light absorption, generation, separation and reactivity) of the photogenerated charge-
295 carriers. Not all the factors can be estimated with the above-mentioned electrochemical measurements,
296 such as the role of crystalline facets exposed and the scattering and absorption efficiencies, and the
297 adsorption of substrates and reaction intermediates, although this last was ruled out before.[27-29]
298 However, the results of electrochemistry can help in decoupling some of these different factors, and in
299 particular the reactivity of charge carriers. With this aim we measured the perturbation of the OCP upon
300 the addition of different amounts of methanol.

301 After the addition of methanol, the OCP shifted to more negative values (OCP3 and OCP 4 in Table 1),
302 demonstrating that photogenerated holes are reactive towards organics such as methanol. Indeed, the hole
303 reaction with methanol reduced steady state concentration of holes and therefore also the photoelectron
304 recombination rate, which ultimately led to the OCP cathodic shift. This cathodic shift was proportional to
305 the methanol concentration in the electrolyte. Nevertheless, we detected a saturation effect of the
306 methanol concentration, especially for the undoped sample, for which we observed a cathodic shift of only
307 5 mV increasing methanol concentration from 60 to 600 mM. Owing to this saturation effect, and keeping
308 in mind that the most negative OCP reachable under irradiation is the E_{FB}, [30] we considered the OCP
309 under irradiation in the presence of 600 mM CH_3OH as an estimation of the E_{FB} for the materials under
310 investigation (E_{FB} in Table 1). This estimate is legitimate because the light intensity used was moderate (84
311 W m^{-2} in the UV), electron scavengers were excluded (to favor photoelectron accumulation), recombination
312 rates were relatively low and further reduced upon the addition of a hole scavenger such as 600 mM
313 CH_3OH. Other procedures for E_{FB} estimation could not be employed in this case. Considering the porous
314 morphology of ZnO electrodes, their capacitance would not behave ideally, and therefore the Mott-
315 Schottky plots would deviate significantly from linearity,[24, 31] impeding the extraction of E_{FB} and donor

density with this strategy. Translating the E_{FB} obtained at pH 0 vs NHE (Table 1), we were able to compare E_{FB} with water reduction potential. Since E_{FB} values obtained at pH 0 vs NHE were positive, we concluded that ZnO and doped ZnO cannot promote photocatalytic water reduction and hydrogen production, as opposed to TiO_2 P25. The E_{FB} values for ZnO materials were comprised between 92 and 262 mV vs NHE at pH 0, showing an anticorrelation between E_{FB} and $k_{2,O2}$ (r=0.70) and $k_{1,O2}$(r=0.61). We remember that the critical value for the correlation constant r is r = 0.608 at 0.10 significance level for 4 degrees of freedom. Being the correlations found larger than 0.608, the null hypothesis (no influence of E_{FB} on k_{O2}) could be discarded with 90% confidence. Four degrees of freedom were considered as the degrees of freedom are the number of data couples minus two (in this case the six couples E_{FB}, k_{O2}). The anticorrelation suggests that the potential of the conduction band influences photoelectron transfer rate, and, therefore, if photoelectron transfer were rate-limiting, E_{FB} might also play a role during the photocatalytic degradation of organic compounds.

Another important piece of information was gathered taking into account the photocurrents recorded at potentials 400 and 800 mV more positive than E_{FB} (I_{ph}400 and I_{ph}800 in Table 1). These potentials were chosen to compare different semiconductors in the same conditions, because it is known that photocurrent vanishes approaching E_{FB}. [30, 32] Moreover, comparing the photocurrents at two different potentials, we were able to assess the effect of the external bias on photocurrent density. The photocurrents were anodic for all the samples, confirming that the materials studied are n-type semiconductors. In this case ZnO-Er presented the largest photocurrents, while the lowest values were recorded in the cases of undoped ZnO and ZnO-Pr. Nevertheless, it is not possible to order unambiguously the materials with the photocurrent, because the order is different as a function of the potential applied. There is a 3-fold increase in the case of ZnO-La and ZnO-Er from E_{FB} + 400 mV to E_{FB} + 800 mV, whereas it is almost constant for TiO_2 P25 and ZnO-Yb. Other cases are intermediate.

With the help of electrochemical tests we verified that for ZnO specimens the photocatalytic activity stems from charge carrier separation upon irradiation and their reactivity with solution species (organics such as methanol in the case of holes, and O_2 in the case of electrons). Nevertheless, from these data a complex picture emerged, where there was not an electrochemical variable clearly responsible for the photocatalytic rates observed. In these cases, considering two parameters at the time may result in incomplete or misleading analysis of the results. For this reason, we undertook a partial least square (PLS) analysis, in which the observed kinetic constants were expressed as functions of the electrochemical parameters previously evaluated (Table 1). PLS is particularly suitable for this task, because it is not adversely affected by collinear variables.

PLS analysis suggests that two PCs (principal components) are sufficient to predict the photocatalytic rates, explaining 65 and 6% of the rate variance, respectively. From the analysis of the regression coefficients on

PC1 and PC2 we observed that all the experimental electrochemical variables contributed significantly to PCs (Figure S11), with the exception of the OCP recorded in dark, which was not relevant for the photodegradation experiments. Moreover, the absolute values of the regression coefficients were similar for both PC1 and PC2. More pronounced differences in the regression coefficients of each parameter are present in the case of PC2, as a function of the type of water used.

The observed rates (see Figure S12, reporting x and y loading weights) are strongly correlated to photoelectron densities recorded in N_2 purged electrolyte (i.e. $n_{ph}2$, $n_{ph}3$ and $n_{ph}4$, Table 1) and then are linked to the absorption of the materials at $\lambda < 400$ nm. From the analysis of scores and loadings of the electrochemical variables only (Figure 4) we infer that PC1 reflects $n_{ph}2$, $n_{ph}3$ and $n_{ph}4$, i.e. the photoelectron densities recorded in N_2 purged electrolyte with and without CH_3OH, while PC2 reflects $n_{ph}5$ and E_{FB}. ZnO-Yb displays a strong PC1 component. It is strongly correlated to $n_{ph}3$ and $n_{ph}4$, thus suggesting that Yb doping is beneficial for photoelectron accumulation.

The rates in MilliQ and waste water have very similar coordinates on PC1 and are only differentiated on PC2. Because PC2 depends on E_{FB}, we conclude that larger reactivity on wastewater matrices is due to a more positive E_{FB}, which implies a more positive valence band potential, and, therefore, more oxidizing holes.

ZnO-Er lies at relatively high value of PC1 (as ZnO-Yb, see Figure 4) but at positive values of PC2. It is well correlated to $I_{ph}800$ (and $I_{ph}400$). Therefore, doping with Er promotes a positive E_{FB}, a large photocurrent value, and, indeed, large photoelectron accumulation. Conversely, ZnO-Ce displays slightly positive coordinate on PC1, markedly negative on PC2 (as ZnO-Yb), and strongly correlates with k_R and $k_{1,O2}$. Ce doping makes E_{FB} more negative, with a large increase in the charge transfer kinetics to dissolved oxygen. In this case we can affirm that there is an improved charge carrier separation. The doping with La and Pr does not significantly modify the performance compared with pristine ZnO. These specimens have negative values of PC1, with null contribution from PC2. Compared with Ce, Er and Yb doping, these specimens have lower photoelectron accumulation ability. Thus, PLS analysis effectively summarizes all the electrochemical and photodegradation data and allows an interpretation of the role of each specific dopant: limited role for La and Pr, improved photocurrent for Er, better accumulation of photoelectrons for Yb and faster electron transfer for Ce.

4. Conclusions

Lanthanide-doped ZnO proved to be very effective in the degradation of pollutants, especially in real wastewater matrices, where they outperformed the benchmark TiO_2 P25. Doping with Yb makes ZnO a robust and efficient photocatalyst. The photoactivity probed with electrochemical techniques correlates well with the photocatalytic activity in the degradation of model pollutants, also in matrices relevant for

real world application, especially when the photoelectron accumulation and charge carrier separation properties are considered. Electrochemical evidences demonstrated how the photocatalytic activity stems from a combination of different effects, often with opposite weight, i.e. the photoelectron density, the conductivity of the interface (photocurrent, reactivity of electron with oxygen and of holes here determined in the presence of methanol), and the recombination of charge carriers. When the combination of these effects (absorption, catalytic and electronic) leads to positive results an improved electron-hole separation effect is often loosely invoked. Conversely, the doping with rare earth elements affects differently many important physical and chemical properties of ZnO such as: *i)* the light absorption properties, which affect the photoelectron density and the photocurrent; *ii)* the recombination and O_2 reactivity constants; and, eventually, *iii)* the flat band potential, which determines the reactivity of the photogenerated electrons.

Acknowledgments

This Special Issue is dedicated to honor the retirement of Prof. César Pulgarin at the Swiss Federal Institute of Technology (EPFL, Switzerland), a key Figure in the area of Catalytic Advanced Oxidation Processes. We also acknowledge support by MIUR, in the frame of the international consortium WATERJPI2013-MOTREM of the "Water Challenges for a Changing World" Joint Programming Initiative (WaterJPI) Pilot Call and ACEA Pinerolese for providing water samples.

Figures

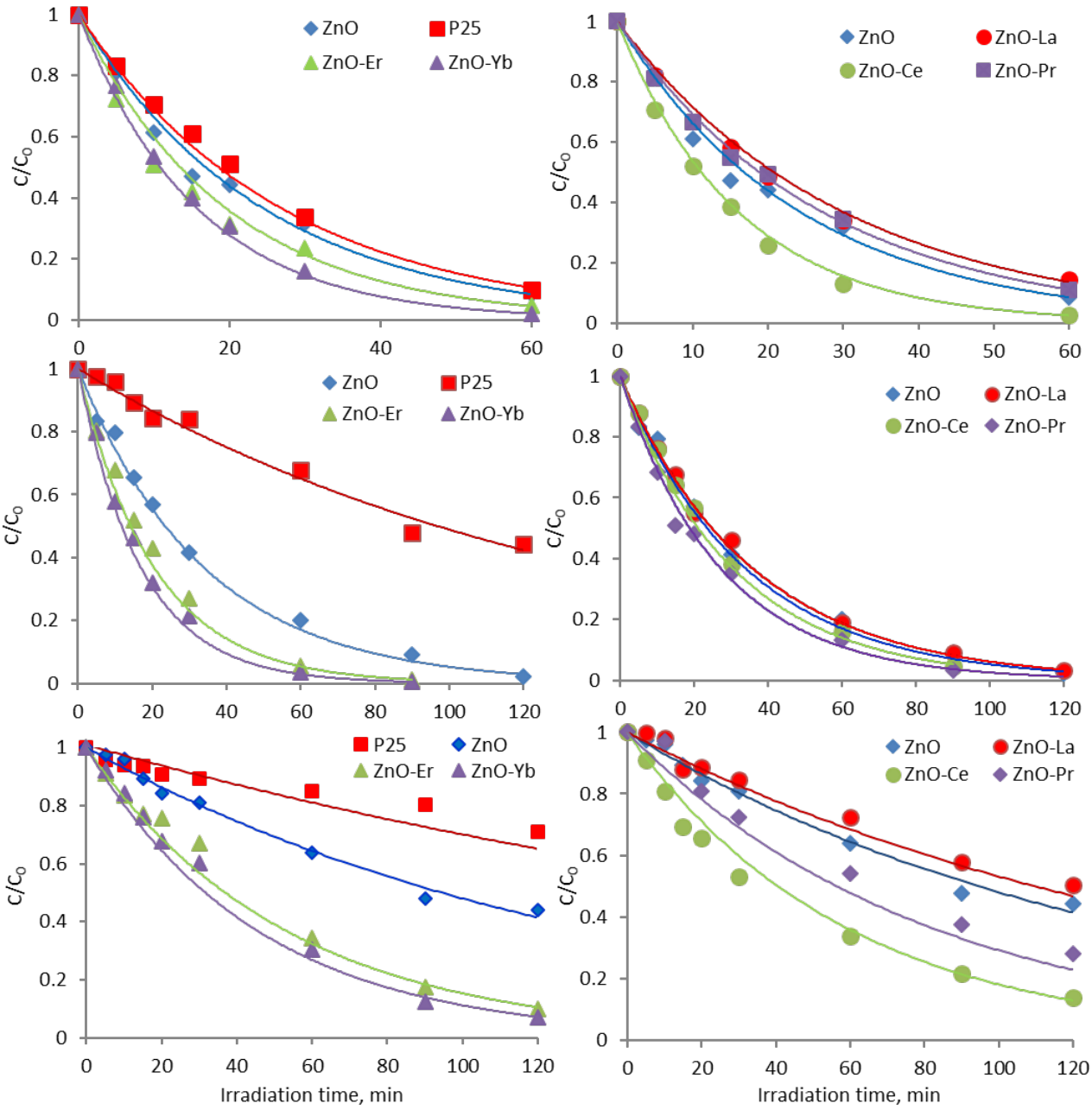

Figure 1. Phenol degradation curves in the presence of different catalysts under UV-A light in MilliQ water (top), EWW (middle) and IWW (bottom).

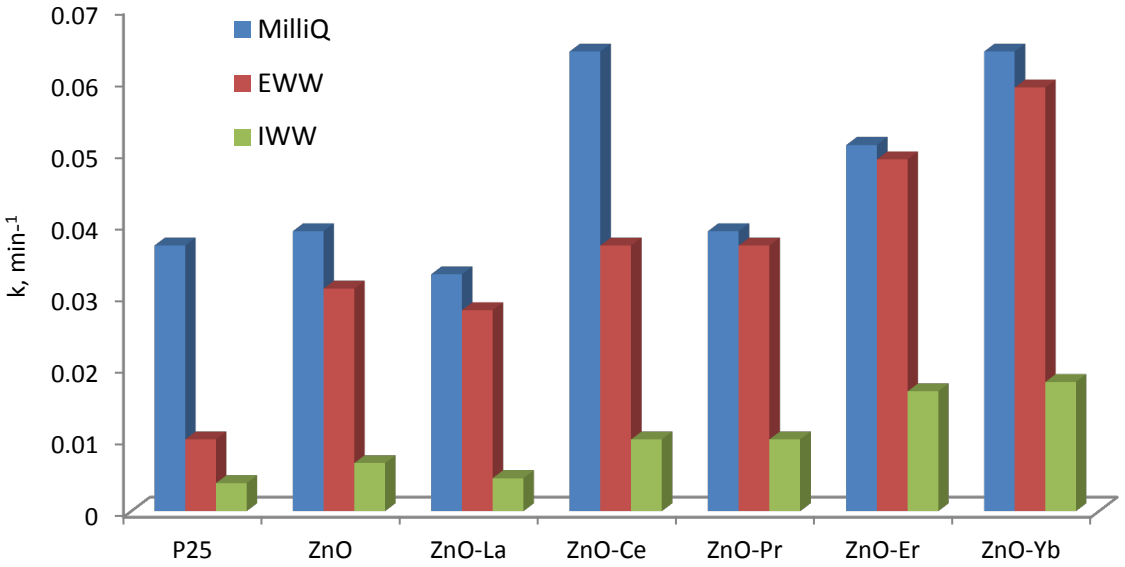

408

409 **Figure 2**. Kinetic constants (k) calculated in ultrapure water (■), EWW (■) and IWW (■). Numerical data are
410 reported in Table 1.

411

412

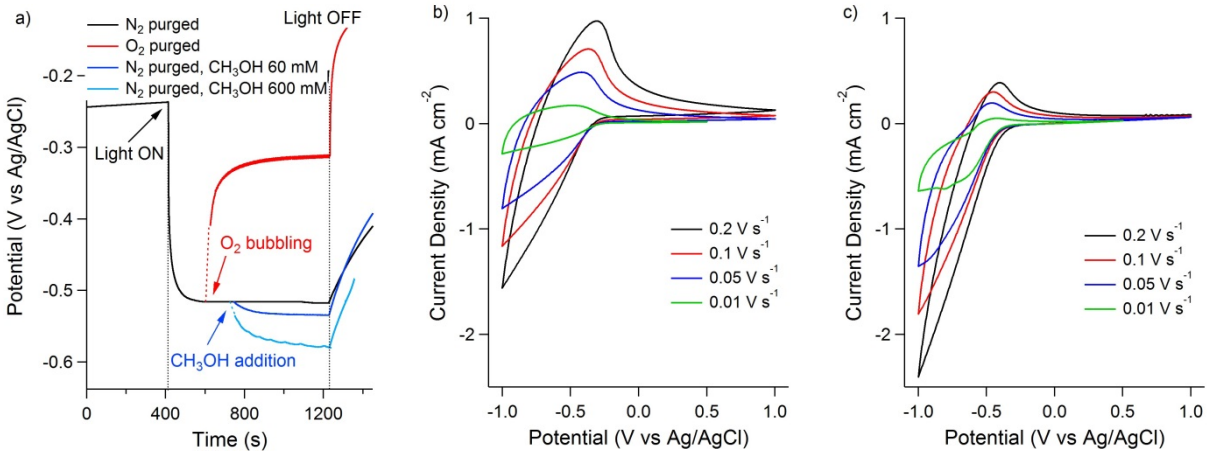

413 **Figure 3**. Chronopotentiometries under different conditions (a) and cyclic voltammetries at different
414 potential scan rates of ZnO in N_2 (b) and O_2 (c) purged electrolytes.

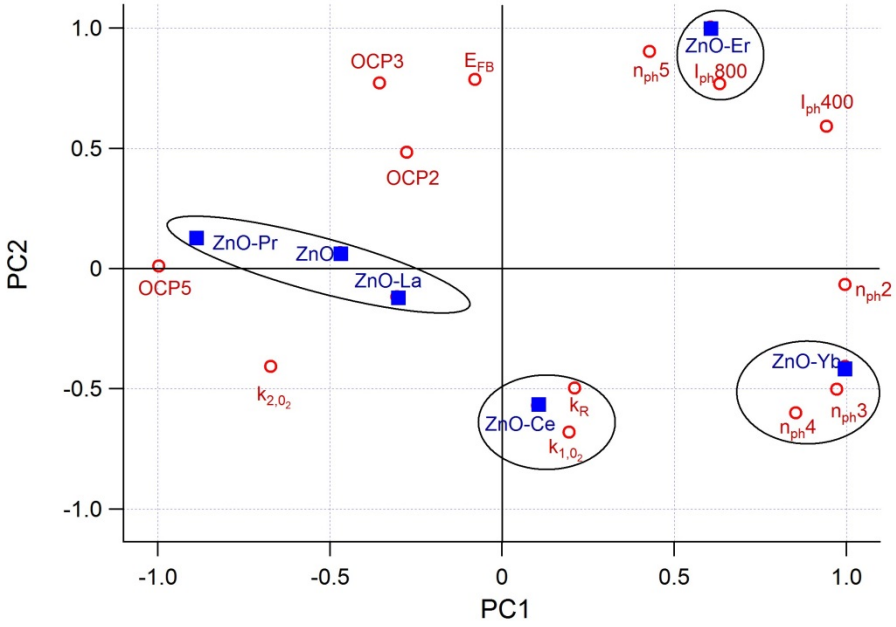

Figure 4. Score and loading weights of the electrochemical variables in the PC plane. PC1 and PC2 explain 65 and 6% of variance, respectively. Circles gather together correlated variables and samples, as presented in the discussion section.

Table 1. Open circuit potential values (vs Ag/AgCl, unless otherwise stated) in different electrolytes and photocurrent values obtained from CV under N_2 purge at scan rate 10 mV s^{-1}; photoelectron densities (cm^{-3}) in different electrolytes and rate constants (s^{-1}) for recombination and reaction with O_2 for P25, pristine and doped ZnO; the last 3 rows report the first order degradation constants for phenol, already plotted in Figure 2.

Acronym	Conditions	ZnO	ZnO-La	ZnO-Ce	ZnO-Pr	ZnO-Er	ZnO-Yb	TiO_2 P25
OCP1	Dark, N_2 purged, mV	-9.5	-172	-103.2	173	-9.5	-190.5	-67
OCP2	Light, N_2 purged ($OCP_{N2, light}$), mV	-515.0	-444.7	-441.2	-452.7	-415.6	-545.3	-773.4
OCP3	Light, N_2 purged, CH_3OH 60 mM, mV	-529.8	-505.5	-513.0	-480.2	-436.6	-589.8	-875.9
OCP4	Light, N_2 purged, CH_3OH 600 mM (E_{FB} pH 8.85), mV	-579.8	-565.1	-542.5	-529.8	-454.6	-624.5	-922.6
OCP5	Light, O_2 purged, ($OCP_{O2, light}$), mV	-314.4	-273	-269.6	-167.0	-320	-361	-122
$I_{ph}400$	Photocurrent at E_{FB} + 400 mV, µA	8±1	8±2	15±1	8±1	35±5	20±1	15±2
$I_{ph}800$	Photocurrent at E_{FB} + 800 mV, µA	15±2	25±5	25±2	11±1	85±5	21±2	15±1
E_{FB}	E_{FB} pH 0 vs NHE, mV	139.9	154.1	176.7	176.4	262.2	92.3	-200.5
$n_{ph}2$	Light, N_2 purged, cm^{-3}	$1.4\cdot10^{17}$	$2.0\cdot10^{17}$	$1.3\cdot10^{17}$	$1.2\cdot10^{17}$	$2.0\cdot10^{17}$	$3.1\cdot10^{17}$	$0.4\cdot10^{17}$
$n_{ph}3$	Light, N_2 purged, CH_3OH 60 mM, cm^{-3}	$1.6\cdot10^{17}$	$2.8\cdot10^{17}$	$3.1\cdot10^{17}$	$1.5\cdot10^{17}$	$2.2\cdot10^{17}$	$4.7\cdot10^{17}$	$1.5\cdot10^{17}$
$n_{ph}4$	Light, N_2 purged, CH_3OH 600 mM (E_{FB} pH 8.85), cm^{-3}	$1.9\cdot10^{17}$	$3.9\cdot10^{17}$	$4.2\cdot10^{17}$	$2.0\cdot10^{17}$	$2.4\cdot10^{17}$	$6.1\cdot10^{17}$	$2.7\cdot10^{17}$
$n_{ph}5$	Light, O_2 purged, cm^{-3}	$4.5\cdot10^{16}$	$2.5\cdot10^{16}$	$1.0\cdot10^{16}$	$1.4\cdot10^{16}$	$12.5\cdot10^{16}$	$1.9\cdot10^{16}$	$0.1\cdot10^{16}$
k_R	k_R @ $1.0\cdot10^{17}cm^{-3}$, s^{-1}	$2.5\cdot10^{-3}$	$1.1\cdot10^{-3}$	$35\cdot10^{-3}$(extr)	$0.8\cdot10^{-3}$	$2.8\cdot10^{-3}$	$5.0\cdot10^{-3}$	$4\cdot10^{-3}$ (a)
$K_{2,R}$	k_R @ $OCP_{N2, light}$, s^{-1}	$3.2\cdot10^{-3}$	$2.6\cdot10^{-3}$	$10.0\cdot10^{-3}$	$2.5\cdot10^{-3}$	$6.1\cdot10^{-3}$	$3.7\cdot10^{-3}$	$2.5\cdot10^{-3}$
$K_{1,O2}$	k_{O2}@ $1.0\cdot10^{16}cm^{-3}$, s^{-1}	0.03·	0.17	0.10	0.04	0.001	0.13	0.15(a)
$K_{2,O2}$	k_{O2}@ $OCP_{O2, light}$, s^{-1}	0.25	0.27	0.10	0.20	0.03	0.18	0.02
kW	In MilliQ water, min^{-1}	0.039	0.033	0.064	0.039	0.051	0.064	0.037
kE	In EWW, min^{-1}	0.031	0.028	0.037	0.037	0.049	0.059	0.01
kI	In IWW, min^{-1}	0.0067	0.0046	0.01	0.01	0.0167	0.018	0.0039

a) extrapolated

References

[1] A.A. Ismail, A. El-Midany, E.A. Abdel-Aal, H. El-Shall, Application of statistical design to optimize the preparation of ZnO nanoparticles via hydrothermal technique, Mater. Lett. 59 (2005) 1924-1928.

[2] W. Zhang, Z. Zhong, Y. Wang, R. Xu, Doped solid solution: $(Zn_{0.95}Cu_{0.05})_{1-x}Cd_xS$ nanocrystals with high activity for H_2 evolution from aqueous solutions under visible light, J. Phys. Chem. C 112 (2008) 17635-17642.

[3] R. Kumar, A. Umar, G. Kumar, M.S. Akhtar, Y. Wang, S.H. Kim, Ce-doped ZnO nanoparticles for efficient photocatalytic degradation of direct red-23 dye, Ceram. Int. 41 (2015) 7773-7782.

[4] D. Sarkar, C.K. Ghosh, S. Mukherjee, K.K. Chattopadhyay, Three dimensional Ag_2O/TiO_2 type-II (p–n) nanoheterojunctions for superior photocatalytic activity, ACS Appl. Mat. Interfaces 5 (2012) 331-337.

[5] M. Li, W. Wu, K. Liu, G. Hu, H. Xu, Three-dimensional assembly and electrical properties of Cu_2O/ZnO heterojunction via an electrochemical superfilling method, Electrochim. Acta 71 (2012) 100-105.

[6] L. Ma, H. Fan, H. Tian, J. Fang, X. Qian, The n-ZnO/n-In_2O_3 heterojunction formed by a surface-modification and their potential barrier-control in methanal gas sensing, Sensors and Actuators B: Chemical 222 (2016) 508-516.

[7] G. Mohamed Reda, H. Fan, H. Tian, Room-temperature solid state synthesis of Co_3O_4/ZnO p–n heterostructure and its photocatalytic activity, Adv. Powder Technol. 28 (2017) 953-963.

[8] C. Gionco, M.C. Paganini, E. Giamello, R. Burgess, C. Di Valentin, G. Pacchioni, Cerium-Doped Zirconium Dioxide, a Visible-Light-Sensitive Photoactive Material of Third Generation, J. Phys. Chem. Lett. 5 (2014) 447-451.

[9] C. Jayachandraiah, G. Krishnaiah, Influence of cerium dopant on magnetic and dielectric properties of ZnO nanoparticles, J. Mater. Sci. 52 (2017) 7058-7066.

[10] O. Bechambi, A. Touati, S. Sayadi, W. Najjar, Effect of cerium doping on the textural, structural and optical properties of zinc oxide: Role of cerium and hydrogen peroxide to enhance the photocatalytic degradation of endocrine disrupting compounds, Mater. Sci. Semicond. Process. 39 (2015) 807-816.

[11] E. Cerrato, C. Gionco, M.C. Paganini, E. Giamello, E. Albanese, G. Pacchioni, Origin of Visible Light Photoactivity of the CeO_2/ZnO Heterojunction, ACS Applied Energy Materials 1 (2018) 4247-4260.

[12] P. Calza, C. Gionco, M. Giletta, M. Kalaboka, V.A. Sakkas, T. Albanis, M.C. Paganini, Assessment of the abatement of acelsulfame K using cerium doped ZnO as photocatalyst, J. Hazard. Mater. 323 (2016) 471-477.

[13] M.C. Paganini, D. Dalmasso, C. Gionco, V. Polliotto, L. Mantilleri, P. Calza, Beyond TiO_2: Cerium-Doped Zinc Oxide as a New Photocatalyst for the Photodegradation of Persistent Pollutants, ChemistrySelect 1 (2016) 3377-3383.

[14] E. Cerrato, C. Gionco, I. Berruti, F. Sordello, P. Calza, M.C. Paganini, Rare earth ions doped ZnO: Synthesis, characterization and preliminary photoactivity assessment, J. Solid State Chem. 264 (2018) 42-47.

[15] N. Yao, J. Huang, K. Fu, S. Liu, E. Dong, Y. Wang, X. Xu, M. Zhu, B. Cao, Efficiency enhancement in dye-sensitized solar cells with down conversion material ZnO: Eu^{3+}, Dy^{3+}, J. Power Sources 267 (2014) 405-410.

[16] M. Faisal, A.A. Ismail, A.A. Ibrahim, H. Bouzid, S.A. Al-Sayari, Highly efficient photocatalyst based on Ce doped ZnO nanorods: Controllable synthesis and enhanced photocatalytic activity, Chem. Eng. J. 229 (2013) 225-233.

[17] P.V. Korake, R.S. Dhabbe, A.N. Kadam, Y.B. Gaikwad, K.M. Garadkar, Highly active lanthanum doped ZnO nanorods for photodegradation of metasystox, J. Photochem. Photobiol. B Biol. 130 (2014) 11-19.

[18] A.S. Weber, A.M. Grady, R.T. Koodali, Lanthanide modified semiconductor photocatalysts, Catal. Sci. Technol. 2 (2012) 683-693.

[19] V. Augugliaro, L. Palmisano, A. Sclafani, C. Minero, E. Pelizzetti, Photocatalytic degradation of phenol in aqueous titanium dioxide dispersions, Toxicol. Environ. Chem. 16 (1988) 89-109.

[20] P.A. Connor, K.D. Dobson, A.J. McQuillan, New Sol-Gel Attenuated Total Reflection Infrared Spectroscopic Method for Analysis of Adsorption at Metal Oxide Surfaces in Aqueous Solutions. Chelation of TiO_2, ZrO_2, and Al_2O_3 Surfaces by Catechol, 8-Quinolinol, and Acetylacetone, Langmuir 11 (1995) 4193-4195.

[21] X.J. Li, J.W. Cubbage, W.S. Jenks, Photocatalytic degradation of 4-chlorophenol. 2. The 4-chlorocatechol pathway, J. Org. Chem. 64 (1999) 8525-8536.

[22] C. Minero, G. Mariella, V. Maurino, E. Pelizzetti, Photocatalytic Transformation of Organic Compounds in the Presence of Inorganic Anions. 1. Hydroxyl-Mediated and Direct Electron-Transfer Reactions of Phenol on a Titanium Dioxide−Fluoride System, Langmuir 16 (2000) 2632-2641.

[23] F. Fabregat-Santiago, I. Mora-Sero, G. Garcia-Belmonte, J. Bisquert, Cyclic voltammetry studies of nanoporous semiconductors. Capacitive and reactive properties of nanocrystalline TiO_2 electrodes in aqueous electrolyte, J. Phys. Chem. B 107 (2003) 758-768.

[24] F. Sordello, V. Maurino, C. Minero, Photoelectrochemical study of TiO_2 inverse opals, J. Mater. Chem. 21 (2011) 19144 - 19152.

[25] Y.-R. Luo, R.H. Byrne, The Influence of Ionic Strength on Yttrium and Rare Earth Element Complexation by Fluoride Ions in $NaClO_4$, $NaNO_3$ and NaCl Solutions at 25 °C, Journal of Solution Chemistry 36 (2007) 673.

[26] D. Monllor-Satoca, R. Gomez, Electrochemical Method for Studying the Kinetics of Electron Recombination and Transfer Reactions in Heterogeneous Photocatalysis: The Effect of Fluorination on TiO_2 Nanoporous Layers, J. Phys. Chem. C 112 (2007) 139-147.
[27] C. Minero, D. Vione, A quantitative evalution of the photocatalytic performance of TiO_2 slurries, Appl. Catal. B: Environ. 67 (2006) 257-269.
[28] T. Ohno, K. Sarukawa, M. Matsumura, Crystal faces of rutile and anatase TiO_2 particles and their roles in photocatalytic reactions, New J. Chem. 26 (2002) 1167-1170.
[29] F. Pellegrino, L. Pellutiè, F. Sordello, C. Minero, E. Ortel, V.-D. Hodoroaba, V. Maurino, Influence of agglomeration and aggregation on the photocatalytic activity of TiO_2 nanoparticles, Appl. Catal. B: Environ. 216 (2017) 80-87.
[30] R. Beranek, (Photo)electrochemical Methods for the Determination of the Band Edge Positions of TiO_2-Based Nanomaterials, Advances in Physical Chemistry 2011 (2011) 786759.
[31] B.H. Ernè, D. Vanmaekelbergh, J.J. Kelly, Morphology and strongly enhanced photoresponse of GaP electrodes made porous by anodic etching, J. Electrochem. Soc. 143 (1996) 305-314.
[32] M.A. Alpuche-Aviles, Y. Wu, Photoelectrochemical Study of the Band Structure of Zn_2SnO_4 Prepared by the Hydrothermal Method, J. Am. Chem. Soc. 131 (2009) 3216-3224.